Assessing girth weld quality of pipeline steels and their susceptibility to hydrogen embrittlement

Zachary N. Buck[1], Newell Moser[1], Nicholas Derimow[1], May L. Martin[1], Damian Lauria[2], Enrico Lucon[1], Douglas Stalheim[3], Peter Bradley[1], Matthew Connolly[1]*

[1]Applied Chemicals and Materials Division, National Institute of Standards and Technology (NIST), Boulder, CO, USA
[2] Office of Information Systems Management, National Institute of Standards and Technology (NIST), Boulder, CO, USA
[3] DGS Metallurgical Solutions Inc., Vancouver, WA, USA

ABSTRACT

Hydrogen is known to cause premature failure in various steel infrastructures due to effects of embrittlement, which is particularly detrimental to ferritic steel structures such as pipelines and pressure vessels. Therefore, understanding the susceptibility of these steels to hydrogen embrittlement and the effect of various microstructures found in welds and heat-affected zones (HAZs) is critical for material selection. Here, we report results of mechanical measurements performed in air and in hydrogen of girth welds used in pipeline steels. Fracture toughness was found to be significantly reduced in base, weld and HAZ when measured in gaseous hydrogen. Charpy tests reveal a lower upper shelf energy (USE) of welds compared to base metal, despite exhibiting lower average hardness values for the weld regions, which may be caused by complex microstructure resulting from the welding process.

KEY WORDS: Hydrogen embrittlement, welds, fracture toughness, Charpy testing, hardness mapping

1 INTRODUCTION

Conventional fossil fuels are not only a finite resource for the world's ever-growing energy needs, but they are also known to have a negative impact on the climate, which has presented new challenges among energy sectors to identify environmentally conscious solutions (Baykara, 2018). Hydrogen has long been considered a viable carbon-free option for ever-increasing societal desires to transform our energy infrastructure towards more renewable and alternative technologies (Mazloomi and Gomes, 2012). However, the effects of hydrogen-assisted damage mechanisms that result in the embrittlement of metals, particularly ferritic steels, significantly reduces their lifetime and is a persistent obstacle in designing and manufacturing reliable structural materials for use in energy storage and transportation applications. Ferritic steel pipelines used to transport natural gas are relatively cost effective and easy to manufacture, but are susceptible to embrittlement and subsequent structural failure due to fatigue, reduction in ductility, and fracture when exposed to hydrogen (Martin, *et al*., 2020).

Predicting lifetimes of pipelines can be difficult due to many variables including geography (terranean *vs*. offshore), composition of the gas being transported, and steel grades and welding processes involved in the manufacturing and joining pipelines in the field. Previous measurements on several pipeline steel grades in the presence of gaseous hydrogen have been performed to elucidate the behavior of the base metal fracture resistance (San Marchi, *et al*., 2010, 2011). However, it has not been until more recently that the effects of gaseous hydrogen on the fracture resistance of pipeline welds have been closely investigated (Ronevich, et al., 2021). Despite recent efforts to characterize the fracture resistance of modern and vintage pipeline welds, some inconsistencies remain, which may result from the complicated weld microstructure and processing. The welding processes, in particular, can result in a variety of local chemistries and microstructures, some of which are more susceptible to embrittlement than others. To maintain safe operation of pipelines for hydrogen and/or blended gas mixtures, it is critical to assess the weld qualification requirements when considering new pipeline materials and weld processes, particularly as it relates to fracture properties.

The ASME B31.12 code on Hydrogen Piping and Pipelines (ASME B31.12, 2023) currently provides two options when it comes to design principles for components for hydrogen applications and transportation. The first option, Option A, is a prescriptive materials design method, which limits operating pressures to 21 MPa and 40% of the specified minimum yield strength (SMYS). Such design factors may result in increased wall pipe thickness and ultimate material costs. The second option, Option B, is a more performance-based method, which provides a pathway to increase the pipeline design pressure. However, Option B requires many tests to determine fracture toughness and fatigue crack growth rates (FCGR) in high pressure hydrogen gas, which are expensive and time consuming. However, there is a third option, Option C, being discussed that would provide a suggested range of microstructures that would be less susceptible to degradation by hydrogen. Establishing an Option C requires a great deal of mechanical testing and microstructural characterization of a range of materials, including pipeline welds and alloying elements, their ductility attributes (toughness and Charpy), and maximum though thickness average hardness. To begin addressing this need, the National Institute of

Table 1: Nominal mechanical properties of the base metal and pipeline dimensions of the two materials investigated in this study.

	Material A	**Material B**
Steel Grade	X70M	X65M
Yield Strength (σ_{YS})	542 MPa	510 MPa
Tensile Strength (σ_{TS})	678 MPa	615 MPa
Wall Thickness	15.87 mm	15.87 mm
Outer Diameter	610 mm	610 mm

Standards and Technology (NIST) has been conducting a multi-year study, sponsored by the U.S. Department of Transportation (DOT) and the Pipeline and Hazardous Materials Safety Administration (PHMSA), to investigate the quality of steel pipelines spanning a diverse range of microstructures and grades (Connolly *et al.*, 2023).

Here, we focus on results obtained from fracture toughness, Charpy testing, and Vickers hardness mapping of girth welds from two pipeline materials, which characterize the performance of their base metal, heat-affected zones (HAZs), and welds. Performance benchmarks for this study include determining whether these pipeline components meet criteria outlined in ASME B31.12, such as a minimum fracture toughness of 55 MPa·m$^{1/2}$ and maximum hardness of 235 HV. ASTM E1820 – 23b (ASTM E1820, 2023) fracture toughness tests were performed in air, and in 20.7 MPa high-purity hydrogen to elucidate the quality of these girth welds and how they might be considered under current ASME B31.12 requirements. Additionally, optical microscopy, Charpy testing, and hardness mapping all contribute to this data set and provide insight into the performance of these welds.

2 MATERIAL AND METHODS

The materials used in this study were machined from two API 5L product specification level 2 (PSL2) line pipe steels (API Specification 5L, 2018) and their girths welds, which were processed using shielded metal arc welding (SMAW). Girth welds from the two pipes were made using multiple qualified API 1104 Group 1 and 2 filler metals (API Standard 1104, 2021), which were examined via x-ray radiographs for acceptance criteria outlined in section 9 API 1104.

The mechanical properties of the two pipeline steels and their respective girth welds were measured using fracture toughness, Charpy testing, Vickers hardness mapping. Optical microscopy was also used to characterize girth weld cross sections and resulting fracture surfaces post testing. These steels are representative of modern pipelines that have not yet been in service, and are referred to herein as Material A and Material B. The nominal mechanical properties of each material are shown in Table 1. For both Material A and Material B, the Young's Modulus (E) was 210 GPa and Poisson's Ratio is (υ) was 0.3.

Single-edge notch bend (SE(B)) fracture toughness and standard-size Charpy specimens were machined from three different regions with respect to the girth welds: 1) the base metal, whose compositions are shown in Table 2, 2) the HAZ region corresponding to the outside of fusion line, and 3) the weld region corresponding to the material along the centerline of the weld. The notch for each machined specimen was positioned such that crack propagation would be in the direction of the girth weld (*i.e.*, the circumferential direction of the pipe). The center of the notch for each specimen was positioned near the mid-thickness of pipe and aligned with either the base, weld, or fusion line in the case of the HAZ. Additional information on geometry and notch placement for SE(B) and Charpy specimens are provided in detail by (Moser *et al.*, 2024).

2.1 Hardness Mapping

Vickers hardness measurements were performed using an automated LECO[1] hardness tester (model identification AMH43) on cross sections of the girth welds from Material A and Material B encompassing their respective base metal, HAZ, and weld regions. Sections of each girth weld were hot mounted in a bakelite puck and polished to a mirror finish using 0.05 µm colloidal silica solution. Two-dimensional hardness maps were then obtained from the polished surface of each sample using a grid of approximately 1500 equally spaced indentations. Each indentation was applied under a 500 g load with a dwell time of 13 seconds.

2.2 Charpy Testing

Charpy impact tests were performed in air on base metal, weld, and HAZ of Material A and Material B in accordance with ASTM E23-23a. A machine with ~ 950 J capacity was used to establish full Charpy transition curves over a temperature range of –196 ºC to 125 ºC, revealing the ductile-to-brittle behavior of each material. One measurement was performed at each temperature, except in the case of – 40 ºC, at which three data points were collected. Temperature accuracy was within 3 °C with respect to the nominal value. Transfer times from the cooling/heating medium to the moment of impact were approximately 3 seconds. The impact velocity and radius of the striking edge were 5.5 m/s and 8 mm, respectively.

2.3 Fracture Toughness

Fracture toughness tests were performed on base metal, weld, and HAZ from Material A and Material B girth welds in accordance with ASTM E1820 – 23b. The SE(B) specimens were tested in air and high-purity (99.999%) hydrogen gas environment at a pressure of 20.7 MPa. Measurements performed in hydrogen were done in triplicate whereas just one in-air test was performed for each materials base, weld, and HAZ. Specimens were machined with a geometry that complied with the ASTM E1820 standard with a nominal width (W) of 15.88 mm and thickness (B) of 7.94 mm. Samples were pre-cracked at 10 Hz in air at room temperature, with initial crack sizes approximately 7.93 mm.

Fracture toughness was determined from analyzing force *vs*. crack mouth opening displacement (CMOD) data, which were collected at a displacement rate of 0.001 mm/s, to calculate J-integral resistance curves (J-R curves). Forces were measured using a calibrated 110 kN load cell mounted inside the pressure chamber with CMODs being recorded using a clip-on extensometer. The fracture toughness, J_Q, is defined as the intersection of the J-R curve with a 0.2 mm offset construction line, which has a slope equal to $2\sigma_Y$. Here, the σ_Y is known as the effective yield strength and is defined in E1820 as the average of the yield strength (σ_{YS}) and tensile strength (σ_{TS}). The value of the J-integral at the intersection of the 0.2 mm construction line is labeled J_Q. Plane-strain fracture toughness values J_{Ic}, represents the crack-extension resistance under conditions of crack-tip plane strain. A J_Q result can be qualified as a J_{Ic} if a specific number of qualifications meet validity requirements, as outlined in ASTM E1820.

Table 2: Chemical composition in wt % of Material A and Material B.

Material	**C**	**Si**	**Mn**	**P**	**S**	**V**	**Nb**	**Ti**	**B**
A	0.07	0.28	1.64	0.013	0.003	0.003	0.07	0.02	0.0003
B	0.06	0.33	1.36	0.013	0.003	0.004	0.05	0.004	0.0000

[1]Some commercial equipment and materials are identified in this paper for technical completeness. Such identification is not intended to imply a recommendation or endorsement by NIST or to imply that these products are necessarily the best available for the purpose for which they are employed here.

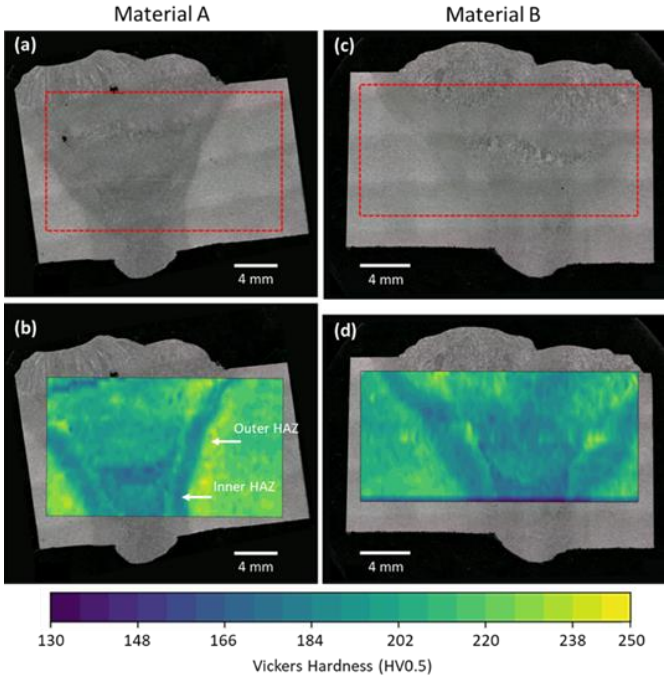

Figure 1: Optical micrographs of the etched surface collected from the cross sections of the girth welds corresponding to (a) Material A and (c) Material B. Hardness maps are superimposed onto the micrographs (b) and (d) and were measured from unetched, but polished surfaces of Material A and B, respectively.

3 RESULTS

3.1 Hardness Mapping

Figure 1 shows optical micrographs of the etched surfaces from Material A and B, in addition to results from 2-dimensional hardness maps obtained from polished surfaces of each material. The red dashed lines in Figure 1(a) and Figure 1(c) represent the area inside which hardness mapping was performed. The hardness maps have been superimposed onto the micrographs (Figure 1(b) and Figure 1(d)) to provide a clear comparison between hardness values and girth weld features. Optical micrographs in Figure 1 were obtained from repolishing away the indentations from hardness mapping and then etching with a 2 % nital solution (2% nitric acid in methanol) to reveal underlying microstructure.

The Vickers hardness (HV0.5) is the most homogeneous within the base metal for each material, which serves as a baseline of hardness isotropy throughout the wrought metal base. Moreover, the overall base hardness of Material A is greater than that of Material B, which correlates well to their steel grade (see Table 1). Evidence of hardness heterogeneity is most present in weld and HAZ regions.

Optical images of Materials A and B (Figure 1(a) and Figure 1(c)) show multiple weld passes within the weld regions that display classic parent austenite columnar morphology of the ferritic grains in the direction of the welding thermal gradient. As these materials were cross sectioned from pipeline girth welds performed in the field by multiple welders, the number of weld passes were not consistent, and the sampled regions do not account for in/out of plane microstructure. Thus, the bulk macrostructure that was characterized consisted of multiple weld regions as well as multiple HAZs. As such, the differences in hardness between these multiple regions can be observed within the superimposed hardness map (Figure 1(b) and Figure 1(d)). From the hardness maps, there appears to be areas of increased hardness along the outer HAZ in Figure 1(b), followed by a significant decrease in hardness within the inner HAZ, indicated by white arrows. The weld regions (areas of rapid solidification) consisted of varying degrees of hardness different from the layered HAZs which can be seen throughout the macrostructure as bands of low hardness scattered throughout. It is likely these regions of the weld contain residual stress from the varying thermal gradients during welding, and the results should therefore be interpreted with consideration given to the fact that these are not singular characteristic weld pools in a controlled environment.

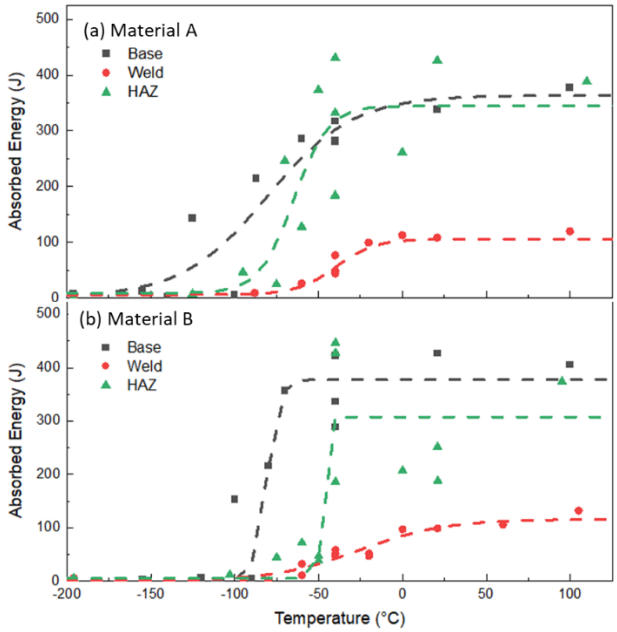

Figure 2: Absorbed energies measured from Charpy base, weld, and HAZ of (a) Material A and (b) Material B tested in air. The dashed lines are fits to the data obtained using a hyperbolic tangent model.

3.2 Charpy

The absorbed energies and resulting transition curves from in-air Charpy measurements collected from base, weld, and HAZ of Material A and Material B are shown in Figure 2. The upper shelf energies (USE) of the base metal from Material A and B were equivalent within the range 355 J – 375 J. However, the welds from both materials exhibit upper shelf energies significantly lower than the base. In both Materials A and B, the HAZ upper shelf energies agree well with those measured from the base metal. However, it is noted that the overall scatter in the HAZ data is high throughout the transition curve. This large scatter of absorbed energies observed from the HAZs may result from several factors. The most common issue is likely due to the fact that these HAZ regions have a microstructure comprised of both fine and coarse grains, which were subjected to a complex thermal history due to

Table 3: Average absorbed energies and their standard deviations from three measurements of each material and region performed at – 40 °C.

	Region	- 40 °C Avg.	stdev
Material A	Base	293.7	16.6
	Weld	54.4	14.6
	HAZ	315.6	101.5
Material B	Base	348.8	55.0
	Weld	52.3	4.7
	HAZ	353.3	118.5

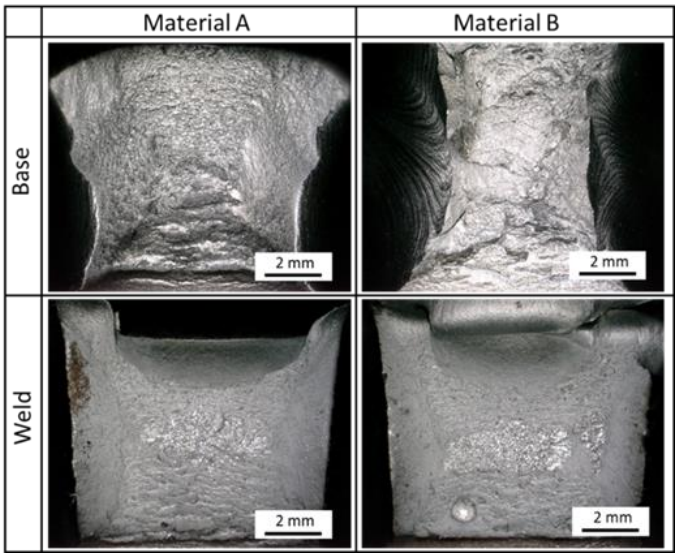

Figure 3: Fracture surfaces of Material A (left) and Material B (right) base (top) and weld (bottom) Charpy specimens tested at room temperature (~ 20.9 ºC).

multiple weld passes. These microstructural phases may be further complicated by starting as-rolled base metal austenite grain size/homogeneity, the presence of Ti and Nb precipitates for austenite grain size control upon welding, overall alloy design hardenability, and/or heat input which typically can be seen in regions of both high and low hardness (Ishikawa, et al., 2022). In addition, due to geometrical constraints, the notch placement could overlap with some base metal. Therefore, the uncertainty in reported USE for HAZ specimens will be greater compared to specimens with notch placement aligned in the base metal and centered on the weld.

Additional evaluation of the data scatter was done at – 40 ºC, which was the only temperature that multiple tests were performed for each material and their respective base, weld and HAZ. Table 3 shows the resulting average absorbed energies and standard deviations from three tests at – 40 ºC performed on each material and region (*ie*., notch placement). For both materials, the HAZ exhibit the greatest uncertainty,

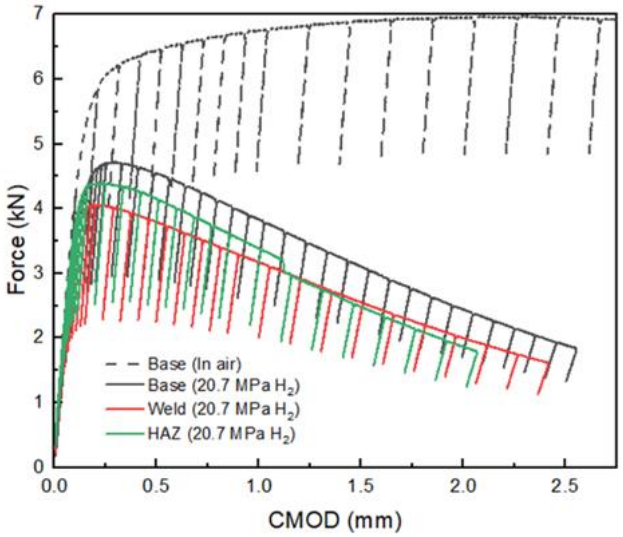

Figure 4: Force *vs.* CMOD curves of the base, weld and HAZ measured on Material B at 20.7 MPa hydrogen. For reference, data from the base material measured in air is shown (black dashed line).

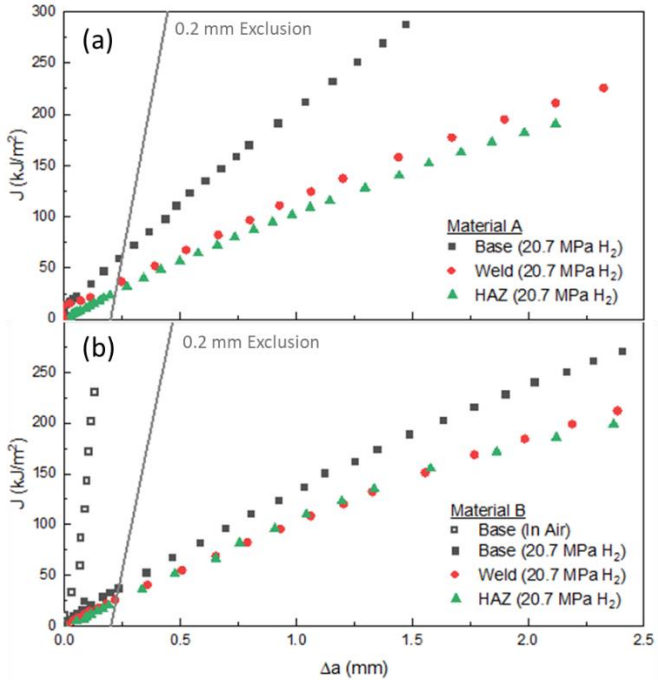

Figure 5: *J-R* curves for (a) Material A and (b) Material B obtained from fracture toughness tests performed in 20.7 MPa hydrogen (closed symbols). The 0.2 mm exclusion line is shown for clarity. Results from in-air tests on Material B base metal are shown (open symbols).

followed by base metal. The absorbed energies from each weld appear to have the least amount of uncertainty, which can be attributed to their overall lower energy profile.

Fits to the absorbed energies were performed using a hyperbolic tangent model (Oldfield, 1975) to construct Charpy transition curves and extract ductile-to-brittle transition temperatures (DBTTs). These fits are shown as dashed lines in Figure 2. For Material A, the DBTTs of base, weld, and HAZ were calculated to be – 80.3 ºC, – 39.6 ºC, and – 64.7 ºC, respectively. The DBTTs for Material B base, weld, and HAZ were – 80.9 ºC, – 25.8 ºC, and – 49.3 ºC, respectively. Despite Material A base metal exhibiting a broad transition from ductile to brittle compared to the sharp transition observed in the base metal of Material B, both have nearly identical DDBT. In the case of weld and HAZ DBTTs measured in Material A, both are shifted to lower temperatures than weld and HAZ measured from Material B.

The fracture surfaces of base and weld Charpy specimens tested at room temperature were imaged and shown in Figure 3. Both base metals appear to be very ductile, as expected from their upper shelf energies (see Figure 2). Despite tests being performed at room temperature (~ 20.9 ºC), and well above the DBTT, the weld surfaces reveal a much more brittle fracture (bottom row of Figure 3). It is noted that the Charpy specimen from base metal of Material A completely broke after impact, whereas the base metal for Material B remained intact.

3.3 Fracture Toughness

Figure 4 shows force *vs.* CMOD measurements collected SE(B) specimens of base, weld, and HAZ from Material B tested at 20.7 MPa hydrogen. For reference, data from an in-air test performed on the base metal is also shown (dashed black line), which was terminated once CMOD reached 4.5 mm. For all three tests in hydrogen, there was a significant decrease in max load and CMOD. These data were used to construct *J-R* curves to quantify fracture toughness. Interestingly, there

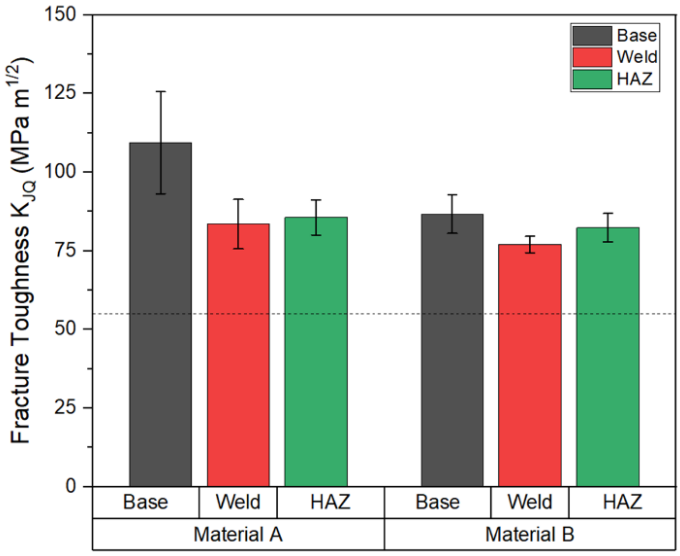

Figure 6: Fracture toughness values K_{JQ} measured from base (black) weld (red) and HAZ (green) specimens of Material A and B in 20.7 MPa hydrogen. Error bars represent the standard deviation measured from multiple tests. The horizontal dashed line indicated the 55 MPa·$m^{1/2}$ lower limit.

is a subtle decrease in load near a CMOD of 1.1 mm for the HAZ specimen that is not present in the base or weld, suggesting a possible unstable crack growth in the HAZ.

Figure 5 shows *J-R* curves for base, weld, and HAZ measured from Material A and B in 20.7 MPa hydrogen. A power law was used to fit qualified points of the *J-R* curves in accordance with ASTM E1820. The J_Q toughness values were determined from the intersection of the data with the 0.2 mm exclusion line (shown as a solid gray line in Figure 5). The J_Q values were successfully extracted from all tests performed in 20.7 MPa hydrogen, however, in-air data was not valid due to the high ductility and limited wall thickness of the pipes. The in-air data of Material B base metal is shown for reference in Figure 5(b), which displays a very steep slope and no intersection with the 0.2 mm exclusion line. Vailed J_Q values were converted to K_{JQ}, which is the classical fracture toughness in mode I – opening mode.

Figure 6 shows average K_{JQ} values measured from repeated fracture toughness tests performed in 20.7 MPa hydrogen of the base, weld, and HAZ on Material A and B. Both base metals from Material A and B exhibit a slightly higher toughness compared to their respective HAZ and welds. In-air tests were also performed for each base, weld and HAZ of Material A and B, however they were found to be non-compliant as they did not pass all the checks outlined in E1820 for K_{JQ} determination. It is estimated, based on geometrical constrains and the maximum measured J_Q that the toughness of Material A and B base metal would exceed 400 MPa·$m^{1/2}$. Regardless of the non-compliant in-air results, it is clear that a significant reduction in toughness occurs for all materials when measured in 20.7 MPa hydrogen gas compared to air.

The fracture surfaces from tested SE(B)s in air and in 20.7 MPa hydrogen are shown in Figure 7. There is significantly limited crack growth and ductile fracture that occurs for in-air tests. The red dashed outline in Figure 7 indicates the area of fracture that occurred during in-air testing of Material B base metal. However, once tested in 20.7 MPa hydrogen gas, the crack growth of base, weld, and HAZ specimens exceeds 2.5 mm when tested in 20.7 MPa hydrogen. This crack length is also evident in *J-R* curves shown in Figure 6. The fracture surfaces that resulted from 20.7 MPa hydrogen testing are indicated with a yellow dashed outline in Figure 7. Interestingly, the HAZ fracture surface imaged from Material B in hydrogen shows regions of heterogeneity, which would likely disrupt crack propagation. The apparent diverse microstructure in this HAZ specimen is further evidence that SE(B) notch placement aligned with the fusion line of these girth welds is difficult and may also explain the subtle decrease in load near a CMOD of 1.1 mm, signifying fracture instability (see Figure 4).

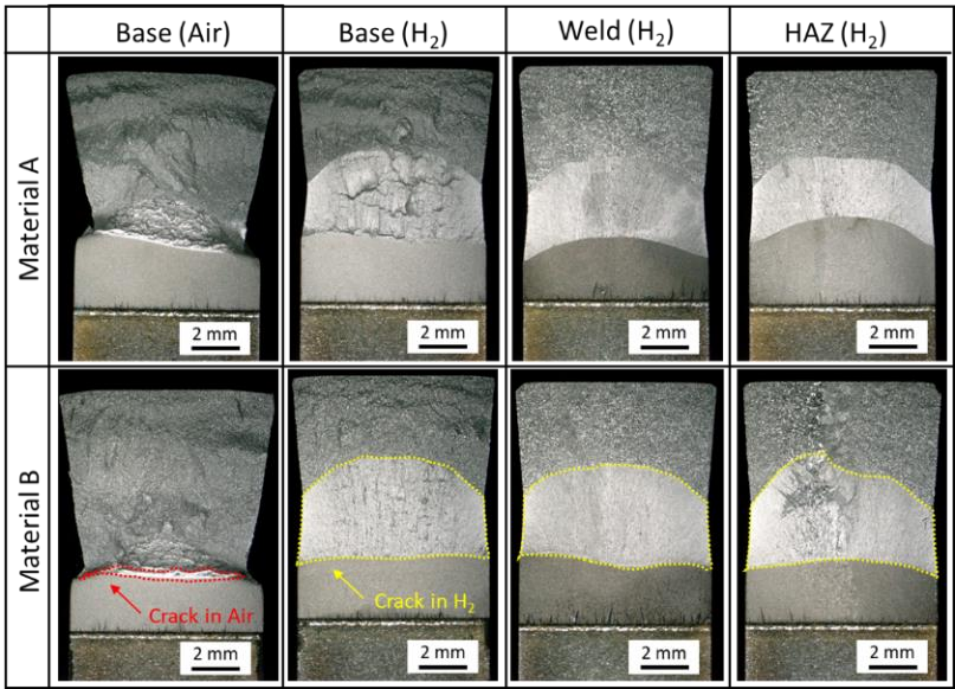

Figure 7: Optical images of the fracture surfaces of the base, weld, and HAZ from Material A (top) and Material B (bottom) in the presence of 20.7 MPa hydrogen. For comparison, the surfaces from in-air tests on base metal of Material A and Material B are also shown (in the left column). The red and yellow dashed lines, respectively, outline the ductile and brittle crack extensions that occurred in air and in hydrogen.

DISCUSSION

Optical microscopy and Vickers hardness maps collected from the girth welds of Material A and Material B reveal large areas of lower hardness within the weld region than the surrounding homogenous base metal. Additional Rockwell hardness measurements were also collected (data not shown) from base and weld metal regions, however, these were unable to distinguish significant differences in hardness between the weld region and base metal. Results from Vickers hardness maps on the higher strength steel (Material B) along the fusion line of the HAZ shows multiple bands of both high and low hardness belonging to the outer and inner HAZ regions, respectively (see Figure 1(b)). This makes notch placement of Charpy and SE(B) HAZ specimens particularly difficult since a propagating crack is likely to encounter multiple microstructures, and possibly sections of weld or base metal as a consequence of the fusion line geometry. Moreover, these girth welds required up to 8 weld passes, which leads to a complex thermal history due to multiple cooling and heating cycles and likely result in a complex microstructure not well defined by a single HAZ. Given that the welds were subjected to many annealing events and varying rates of solidification, we propose that such girth welds should be considered to have multiple heat-affected weld metal regions rather than a homogeneous weld. This is apparent from the contrast observed in the optical images of the etched weld cross sections (Figure 1(a) and Figure 1(c)), which show evidence of multiple melt pools and solidified weld metal. Preliminary results from ongoing measurements using X-ray computed tomography, backscattered electron imaging, and focused ion beam milling, all show evidence of pores present in these welds. However, further study and verification is needed to quantify these pores and how they affect hardness values and Charpy energies.

Data obtained from in-air Charpy tests of HAZs from both Material A and B exhibit significantly more scatter and uncertainty compared to measurements on their base metals and welds, providing further evidence of a complex microstructure. USEs of both Material A and B base metals were ~ 370 J, however the USE of their respective welds decreased to ~ 110 J. This factor of 3 decrease was unexpected as hardness maps of the welds show a lower 0.5HV than their base metal. However, images of the Charpy fracture surfaces (see Figure 3) clearly show a more brittle crack growth for the welds than base metal, which correlates well with a lower USE. We note that the presence of pores in the heat affected weld metal region may explain the lower USE of the weld specimens despite the lower average hardness compared to the more homogenous base metal.

Fracture toughness K_{JQ} values determined from tests performed on base, weld, and HAZs of Material A and B were found to be significantly reduced when measured in 20.7 MPa hydrogen compared to in air. Although for each material, the highest toughness values were measured in the base metal, statistical variation suggests that each of the regions (base, weld, HAZ) would result in a fracture toughness in the range of 75 – 110 MPa·m$^{1/2}$, which is still exceeds the ASME B31.12 minimum of 55 MPa·m$^{1/2}$.

CONCLUSIONS

The quality of two pipeline girth welds were investigated via mechanical testing and optical microscopy techniques. ASTM E1820 fracture toughness tests in air and gaseous hydrogen, Vickers hardness mapping, and ASTM E23-23a Charpy tests in air were performed on the base metals, welds, and HAZs near the girth welds. The following conclusions can be drawn:

1) Two-dimensional Vickers hardness maps collected from cross sections of Material A and Material B reveal lower hardness values for the girth welds than the surrounding base metal. Due to multiple cooling/heating cycles from the welding process, the weld region is more accurately described as a heat-affected weld metal region, which results in complex microstructure and heterogeneities encountered by crack propagation. The HAZ shows regions along the fusion line of both high and low hardness bands, some of which exceed the ASME B31.12 limit of 235 HV.

2) Charpy upper shelf energies for the base metals in Material A and Material B were consistently higher than for their welds – nearly a factor of 3 in both cases. Upper shelf energies were similar between base metals and HAZs, however absorbed energies measured from HAZ specimens contain significant scatter, suggesting a more heterogeneous microstructure and possible overlap with base metal due to the difficulties in notch placement.

3) Hydrogen significantly reduces the fracture toughness of the base, weld, HAZ in Material A and Material B, but still results in values above the minimum 55 MPa·m$^{1/2}$ as required by ASME B31.12. Although compliant toughness values were unattainable from in-air tests, *J-R* curves suggest that this reduction in K_{JQ} could be a factor 5 or more when measured at 20.7 MPa hydrogen.

4) Hardness maps, statistical spread in Charpy energies, and analysis of the fracture surfaces from Material A and B HAZs indicate a complicated microstructure that makes predicting crack propagation difficult compared to the more homogenous base metal.

ACKNOWLEDGEMENTS

The authors thank Dr. Andrew Slifka for his support and insightful discussions on fracture mechanics and hydrogen embrittlement. We wish to acknowledge the Department of Transportation (DOT) Pipeline and Hazardous Materials Safety Administration (PHMSA) for funding this work (Contract # 693JK319N000013-02).

REFERENCES

API Specification 5L (2018). "Specification for Line Pipe," *American Petroleum Institute*.

API Standard 1104 (2021). "Welding of Pipelines and Related Facilities," *American Petroleum Institute*.

ASME B31.12 (2023). "Hydrogen Piping and Pipelines," *ASME Standards and Technology*.

ASTM E1820-23a (2023). "Standard Test Method for Measurement of Fracture Toughness," *ASTM International*.

ASTM E23-23a (2023). "Standard Test Methods for Notched Bar Impact Testing of Metallic Materials," *ASTM International*.

Baykara, SZ (2018). "Hydrogen: A brief overview on its sources, production, and environmental impact," *Int. J. on Hydrogen Energy*, 43: 10605 – 14.

Connolly, MJ, Martin, ML, Buck, ZN, Moser, N, Lucon, E, Lauria, D, Bradley, P, and Slifka AJ (2023). "Determining Steel Weld Qualification and Performance for Hydrogen Pipelines: Phase I Report," *The US Department of Transportation, Pipeline and Hazardous Materials Safety Administration*, 693JK319000013.

Ishikawa, N, Izumi, D, Uranga, P, Isasti, N, Rodriguez-Ibabe, J, Jarreta, D, Martin, D, and Stalheim, D (2022). "Effect of Plate Rolling Strategy and Nb Microalloying in the HAZ Performance after Welding," *Proceedings AISTech.*

Martin, ML, Connolly, MJ, DelRio, FW, and Slifka, AJ (2020). "Hydrogen Embrittlement in Ferritic Steels," *Applied Physics Review*, 7(4), 041301.

Mazloomi, K, and Gomes, C (2012). "Hydrogen as an energy carrier: Prospects and challenges," *Renewable and Sustainable Energy Reviews*, 16: 3025.

Moser, N, Buck, ZN, Derimow, N, Martin, ML, Lauria, D, Lucon, E, Bradley, P, and Connolly, MJ (2024). "Hydrogen embrittlement susceptibility and fracture toughness measurements of welded X65M pipeline steels," *Proc of the ASME 2024 Pressure Vessels and Piping Conference, Bellevue, Washington USA.* PVP2024-122545.

Oldfield, W (1975). "Curve fitting impact test data: A statistical procedure," *Standardization News*, 3(11), 24-29.

Ronevich, JA, Song, EJ, Someday, BP, San Marchi, CW (2021). "Hydrogen-assisted fracture resistance of pipeline welds in gaseous hydrogen," *Int. J. of Hydrogen Energy*, 46, 7601-14.

San Marchi, C, Somerday, BP, Nibur, KA, Stalheim, DG, Boggess, T, Jansto, S (2010). "Fracture and fatigue of commercial grade API pipeline steels in gaseous hydrogen," *Proc of the ASME 2010 Pressure Vessels and Piping Conference, Bellevue, Washington USA.*

San Marchi, C, Somerday, BP, Nibur, KA, Stalheim, DG, Boggess, T, Jansto, S (2011). "Fracture resistance and fatigue crack growth of X80 pipeline steel in gaseous hydrogen," *Proc of the ASME 2011 Pressure Vessels and Piping Conference, Baltimore, Maryland USA.*